

## Laser beam-profile impression and target thickness impact on laser-accelerated protons

M. Schollmeier,<sup>1,2</sup> K. Harres,<sup>1,2</sup> F. Nürnberg,<sup>1,2</sup> A. Blažević,<sup>2</sup> P. Audebert,<sup>3</sup> E. Brambrink,<sup>3</sup> J. C. Fernández,<sup>4</sup> K. A. Flippo,<sup>4</sup> D. C. Gautier,<sup>4</sup> M. Geißel,<sup>5</sup> B. M. Hegelich,<sup>4,6</sup> J. Schreiber,<sup>6</sup> and M. Roth<sup>1,2</sup>

<sup>1</sup>*Technische Universität Darmstadt, Institut für Kernphysik, Schlossgartenstrasse 9, D-64289 Darmstadt, Germany*

<sup>2</sup>*GSI-Gesellschaft für Schwerionenforschung mbH, Plasmaphysik, Planckstr. 1, D-64291 Darmstadt, Germany*

<sup>3</sup>*Ecole Polytechnique, CNRS, CEA, UPMC; Route de Saclay, 91128 Palaiseau, France*

<sup>4</sup>*Los Alamos National Laboratories, Los Alamos, New Mexico 87545, USA*

<sup>5</sup>*Sandia National Laboratories, Albuquerque, New Mexico 87185, USA*

<sup>6</sup>*Department für Physik, Ludwig-Maximilians Universität München, Garching, Germany*

(Received 17 January 2008; accepted 31 March 2008; published online 7 May 2008)

Experimental results on the influence of the laser focal spot shape onto the beam profile of laser-accelerated protons from gold foils are reported. The targets' microgrooved rear side, together with a stack of radiochromic films, allowed us to deduce the energy-dependent proton source-shape and size, respectively. The experiments show, that shape and size of the proton source depend only weakly on target thickness as well as shape of the laser focus, although they strongly influence the proton's intensity distribution. It was shown that the laser creates an electron beam that closely follows the laser beam topology, which is maintained during the propagation through the target. Protons are then accelerated from the rear side with an electron created electric field of a similar shape. Simulations with the Sheath-Accelerated Beam Ray-tracing for Ion Analysis code SABRINA, which calculates the proton distribution in the detector for a given laser-beam profile, show that the electron distribution during the transport through a thick target (50  $\mu\text{m}$  Au) is only modified due to multiple small angle scattering. Thin targets (10  $\mu\text{m}$ ) show large source sizes of over 100  $\mu\text{m}$  diameter for 5 MeV protons, which cannot be explained by multiple scattering only and are most likely the result of refluxing electrons. © 2008 American Institute of Physics.

[DOI: 10.1063/1.2912451]

### I. INTRODUCTION

The irradiation of thin foils with modern ultraintense short-pulse lasers leads to—among other phenomena—the generation of MeV-ion beams.<sup>1–4</sup> These beams contain particle numbers above  $10^{10}$  in the MeV range, are short pulsed ( $\approx$ ps) and, despite their use as a diagnostic (e.g., proton radiography<sup>5–7</sup> or nuclear physics<sup>8</sup>) they could have applications as compact particle accelerators<sup>9</sup> or for proton fast ignition.<sup>10</sup>

Without special target cleaning techniques<sup>11–14</sup> the predominantly accelerated ion species are protons from contamination layers on the target surface.<sup>15</sup> These protons get accelerated because of the buildup of a dense sheath of energetic electrons at the nonirradiated rear surface of the target. The dense sheath results in an electric field on the order of TV/m, which ionizes and accelerates the atoms at the rear side. This acceleration scheme is known as the target normal sheath acceleration (TNSA).<sup>16</sup>

Recently it was shown that target thickness, target composition or laser pulse duration dramatically influence the maximum beam energy and the spectrum.<sup>17–21</sup> The ion beam is always directed normal to the local rear surface of the target with an emittance that is superior compared to conventional accelerator beams.<sup>22–24</sup> The protons are emitted in a laminar fashion with a cone or parabolalike, decreasing angle

of beam-spread with energy.<sup>22,25,26</sup> A prerequisite for the high ion-beam quality is a smooth and hot electron sheath.<sup>22,27</sup>

The hot MeV electrons are created in the laser focus at the front side and were pushed inwards by the laser. The copious amount of MeV electrons results in mega-ampere electron currents that were transported from the front to the rear side of the target. Two- and three-dimensional integrated particle-in-cell simulations of laser-interaction with thin foils (10  $\mu\text{m}$ ) show that the electrons propagate nearly ballistically through the target.<sup>28</sup> However, some of them get a transverse velocity and drift out of the direction given by the laser incidence angle.<sup>29</sup> Experimentally the transport full-cone angle of the electron distribution was determined to be dependent on laser energy intensity as well as target thickness.<sup>30,31</sup> For rather thick targets ( $d > 40 \mu\text{m}$ ) this value is around  $30^\circ$  full width at half maximum (FWHM) (Refs. 32–34) at the laser intensities used in this article, whereas for thin targets published values are in the range of  $16^\circ$  (indirectly obtained by a fit, considering only the maximum proton energy<sup>35,36</sup>) and  $\approx 150^\circ$  at most.<sup>30,33</sup> Just recently, it was shown that different diagnostics lead to different electron transport cone angles,<sup>30</sup> so the question about the “true” cone angle dependence with laser and target parameters still remains unsolved.

The influence of the laser beam profile on proton accel-

eration was discussed in Ref. 34. There a uniform electron transport in gold foils was experimentally found by using laser-accelerated protons as a diagnostics. The authors assumed that the bulk of the hot electrons follows the laser focal spot topology and builds a sheath with the same topology at the rear side. With a simple electrostatic model the proton beam spatial profile, as detected by a film detector, was simulated. The authors took the laser beam profile as an input parameter and assumed the electron transport to be homogeneous, with a characteristic opening angle that needed to be fit to match the measured data. The unknown source size of the protons was fit to best match the experimental results. It was shown, that for their specific target thickness and laser parameters, the fitted broadening angle of the electrons' sheath at the rear side closely matches the broadening angle expected by multiple Coulomb small-angle scattering. However, they could only fit the most intense part of the measured beam and have neglected the lower intense part that originates from rear-side accelerated protons as well. Additionally, there is no information on the dependence of these findings on target thickness.

In this article we therefore did further studies that concentrated on the influence of the transverse laser beam profile on laser-accelerated protons. In one experiment the laser beam profile was stepwise changed from the round, best focused spot to an astigmatic line focus. The influence of the target thickness was probed in another experiment by keeping the laser beam profile constant and by changing the target thickness. In contrast to the experiments described in Ref. 34, we simultaneously measured the source size of the protons by using microgrooved targets similar to those used in Ref. 22. The rear-side microgrooved targets allow, in combination with RCF imaging spectroscopy (RIS),<sup>37</sup> the energy resolved measurement of the transverse beam profile and its source size in one shot.<sup>22,23,26</sup>

The article is organized as follows: Sec. II describes the experimental setup. We show in Sec. III that for rather thick targets ( $50\ \mu\text{m}$ ) the electron transport can be modeled by assuming only multiple small-angle scattering. However, thin targets ( $10\ \mu\text{m}$ ) show a much larger source size than expected, which cannot be explained by scattering only. A discussion of the different broadening mechanisms leads to a conclusion and outlook written in Sec. IV.

## II. EXPERIMENTS

The experiments were performed with the TRIDENT laser system at Los Alamos National Laboratory, NM, USA and the Laboratoire pour l'Utilisation des Lasers Intenses (LULI) 100 TW laser at Ecole Polytechnique, Paris, France. The 30 TW beamline of TRIDENT delivered 25 J in 800 fs on target. The contrast ratio was measured to be  $10^{-6}$  in 2 ns before the main pulse. The laser with a wavelength of  $1.054\ \mu\text{m}$  was incident at a compound (i.e., tip  $19.6^\circ$  and tilt  $22.5^\circ$ ) incident angle of  $\approx 44^\circ$  with respect to the target normal. An  $f/3$  off-axis parabolic mirror focused the pulse to a FWHM focal spot of  $12\ \mu\text{m}$ , leading to an intensity above  $10^{19}\ \text{W}/\text{cm}^2$ . The focal spot was measured with a high resolution, windowless active pixel sensor (APS) in comple-

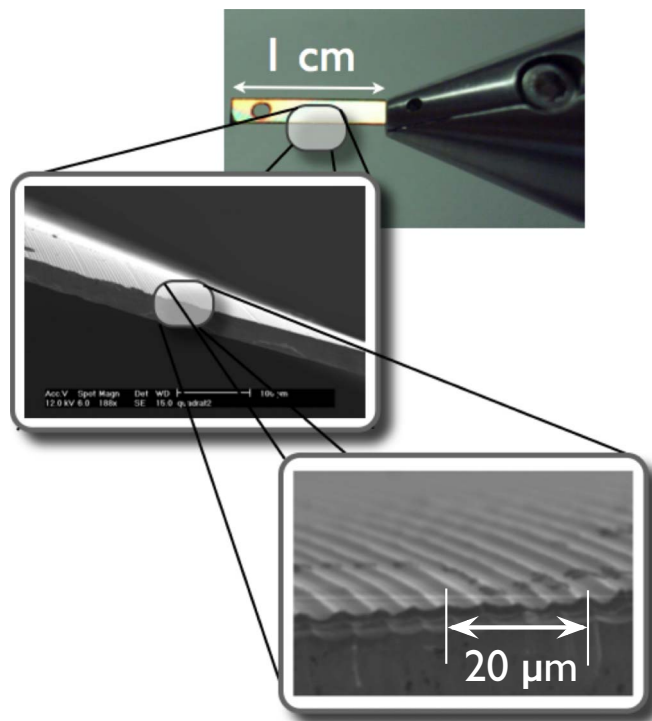


FIG. 1. (Color online) Photography and SEM images of the  $50\ \mu\text{m}$  Au target rear side. Whereas the front surface of the foil is flat, the rear surface was micromachined with a diamond planer to obtain concave lines with a distance of  $5\ \mu\text{m}$  and submicrometer groove depth.

mentary metal oxide semiconductor (CMOS) technology without any optical imaging to avoid misinterpretation of the beam profile due to aberrations. The pixel size of the detector was  $3.5\ \mu\text{m}$  with zero interpixel spacing and allowed to resolve the best focus. The position of the APS surface was accurately controlled with a commercial interferometer to be in the plane of the target surface.

The LULI 100 TW delivered up to 20 J in 300 fs on target at a wavelength of  $1.057\ \mu\text{m}$ . The contrast ratio is  $10^{-6}$  in 500 ps before the main pulse. The laser pulse was focused at normal incidence with an  $f/3$  off-axis parabolic mirror to a FWHM focal spot of  $6\ \mu\text{m}$ , that lead to intensities above  $5 \times 10^{19}\ \text{W}/\text{cm}^2$ . The image of the focus was recorded with a microscope system and a charge coupled device (CCD) camera. In both experiments the laser focus was either best focused or—to measure the influence of its beam profile on the proton beam profile—deformed to an elongated ellipse by tilting the parabolic mirror.

The targets were thin ( $13$ – $50\ \mu\text{m}$ ) gold foils with chamfered, equidistant grooves at the rear side. Due to manufacturing issues, the  $13\ \mu\text{m}$  and  $20\ \mu\text{m}$  thick targets had a rear-side line-spacing of  $10\ \mu\text{m}$ , whereas the  $50\ \mu\text{m}$  thick targets had a line spacing of  $5\ \mu\text{m}$ . All targets had grooves with a depth of less than  $1\ \mu\text{m}$ . Figure 1 shows a photography and scanning electron microscope (SEM) images of the rear side of a  $50\ \mu\text{m}$  thick foil. The microstructure of the rear surface leads to a so called *microfocusing* of the ions that follow the local surface normal in the initial phase of the acceleration.<sup>22</sup> Later on the ion beam expansion follows the global target normal. The microfocusing causes perturbations in the trans-

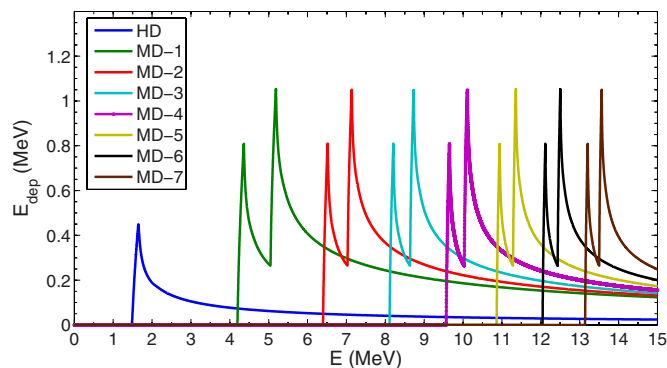


FIG. 2. (Color online) Proton energy deposition response functions of a RadioChromic Film (RCF) stack consisting of one layer of HD-810 and seven layers of MD-55, covered with  $25.4 \mu\text{m}$  aluminum. Due to the unique energy loss characteristics of ions in matter with the Bragg peak at the end of the range, each RCF layer can be attributed to a small energy interval of  $0.5 \text{ MeV}$  for HD-810 and  $1 \text{ MeV}$  for MD-55, respectively.

verse proton flow and those in turn lead to density modulations in the detector.<sup>22,25</sup>

This method of imaging the target surface can be used to directly determine beam properties like real source size, divergence angle, and transverse emittance in a single shot. Additionally, it is possible to reconstruct the shape of the accelerating electron sheath. In order to measure the change of the proton beam-profile with the target thickness, the thickness was systematically increased from  $13$  to  $50 \mu\text{m}$  while keeping the laser parameters constant. For probing the influence of the laser beam profile the target thickness was kept constant at  $50 \mu\text{m}$  and the laser beam was changed as described above.

The accelerated protons were detected with a RadioChromic Film (RCF) stack<sup>38</sup> that was placed behind the target at either  $(23.5 \pm 1) \text{ mm}$  at the TRIDENT or  $(42 \pm 1) \text{ mm}$  at the LULI. The stacks consisted of one layer of type HD-810 and seven layers of MD-55 at the TRIDENT; and one layer of HD-810 and ten layers of MD-55 at the LULI, respectively. Since during the laser-target interaction parasitic

radiation and target debris is created, the RCF stacks were wrapped in  $25.4 \mu\text{m}$  (TRIDENT) or  $17.8 \mu\text{m}$  (LULI) Al-foil for shielding. A RCF is sensitive to all ionizing radiation, but it is most sensitive to protons due to their higher stopping-power compared to electrons or x rays. Heavy ions only penetrate the first layer.

The ions deposit most of their energy at the end of their range in the Bragg-peak, so a stack of RCF layers can be used as a two-dimensionally imaging spectrometer. The energy-loss response functions of protons for the stacks used in these experiments were calculated with a ray-tracing algorithm that uses tabulated energy-loss values from the SRIM-2006 code package.<sup>39</sup> The algorithm divides the whole energy range to be calculated [here (0–15) MeV] into  $0.01 \text{ keV}$  energy bins. Those energies are then used as initial energies. For each initial energy the code subsequently calculates the stopping in every RCF, taking into account the different compositions of the different types. The deposited energy in the active layers is then plotted versus the initial energy. This is shown in Fig. 2. Each layer has a lower detection threshold where the energy deposition quickly rises and then slowly falls off, representing an “inverse” Bragg-curve. MD-55 has two maxima because of the two active layers in the film. Due to this peaked energy deposition profile, every RCF layer can be attributed to a small energy interval with a width of  $1 \text{ MeV}$  for MD-55 and  $0.5 \text{ MeV}$  for HD-810, respectively.

### III. EXPERIMENTAL RESULTS

First we show the results obtained with a round, best focused laser-beam spot. The laser system was the LULI 100 TW. With a nearly diffraction limited laser focal spot, shown in Fig. 3(a), with  $\text{FWHM}=6 \mu\text{m}$ , laser energy  $E_L=15.4 \text{ J}$ , intensity  $I=5.6 \times 10^{19} \text{ W/cm}^2$ , and a target thickness of  $50 \mu\text{m}$  with  $5 \mu\text{m}$  grooves at the rear side, the resulting proton beam is round and smooth; see Fig. 3(b). This is a result of the uniform laser focus as well as a smooth electron transport, first demonstrated by Fuchs *et al.*<sup>34</sup> The microstructured grooves on the target surface were imprinted

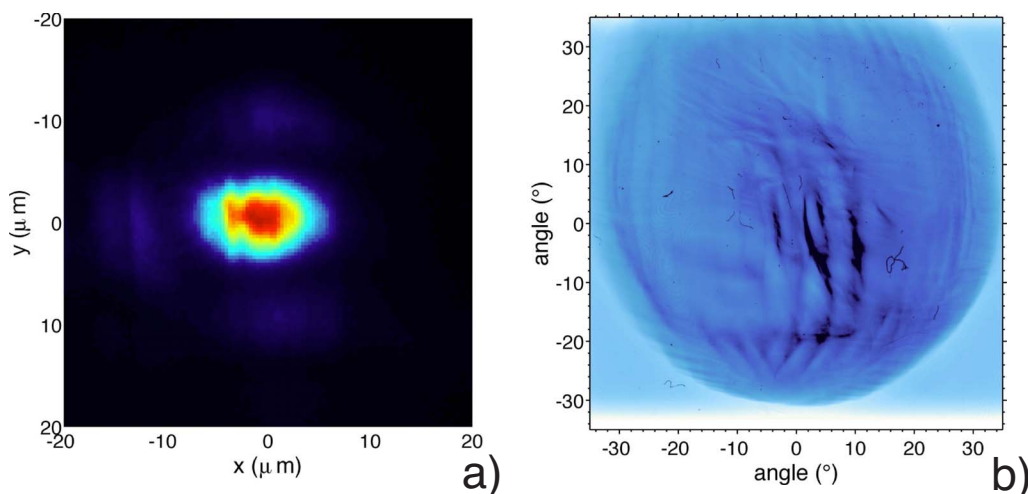


FIG. 3. (Color online) (a) Round laser focus profile (LULI No. 25,  $\text{FWHM}=6 \mu\text{m}$ ,  $E_L=15.4 \text{ J}$ ) that was used to irradiate a  $50 \mu\text{m}$  Au foil. Its rear side grooves with  $5 \mu\text{m}$  distance could be imaged into the RCF that was placed at  $42 \text{ mm}$  distance. (b) The resulting proton beam profile ( $5 \text{ MeV}$ ) is round, and the source size is  $75 \mu\text{m}$ .

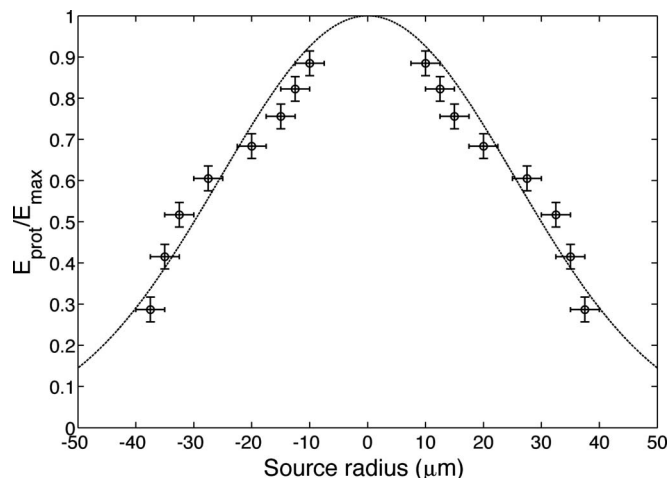


FIG. 4. (LULI No. 25) Source-size dependent energy distribution ( $\circ$ ) from a  $50\ \mu\text{m}$  Au foil, see Fig. 3 for the laser parameters. The plot shows the energies normalized to the maximum energy of 16 MeV. The contrast of the lines did not allow us to deduce the source size of the most energetic protons. The highest resolvable energies were emitted from a source size  $<20\ \mu\text{m}$ . The increasing source size with decreasing energy can be fitted by a Gaussian (---) with  $60\ \mu\text{m}$  FWHM.

in the beam and result in vertical lines with higher dose in the RCF image. The real source size can be derived by counting the lines and by multiplying with the known distance of the surface grooves. This was done for every RCF layer, hence it led to an energy-dependent source size determination. Figure 4 shows the source-size dependent energy distribution ( $\circ$ ), with the energies normalized to the maximum energy of 16 MeV of this shot. The highest energies were emitted from the smallest source. The decrease of the source size with energy exhibits a Gaussian distribution with a FWHM of  $60\ \mu\text{m}$ . These data are comparable to results published in Ref. 22.

Next the laser focus was changed from best focus to a line focus, while the target thickness was kept unchanged. When the laser was defocused to form an elliptical line [Fig.

5(a)], the proton beam profile followed; see Fig. 5(b) of the RCF image of 5 MeV protons. The most intense part of the beam in Fig. 5(b) roughly resembles an ellipse like the laser beam. Note that the orientation of the proton beam ellipse is perpendicular to the laser beam ellipse. This can be understood by following the argument in Ref. 34; the divergence angle of the protons is largest where the gradient of the electron sheath is strongest, that in turn has a similar shape as the laser beam profile. Therefore the transverse acceleration is strongest along the short half-axis of the sheath ellipse and weaker along the long half-axis.

The elliptical part (in one direction) of the 5 MeV protons has four to seven lines, depending on which part of the dark area is assigned to the ellipse. The corresponding source size is then  $(20\text{--}35)\ \mu\text{m}$ , that is very close to the size of the laser focus. Note that even the lower intensity part of the beam shows lines. The visibility of the lines demonstrates that these protons originate from the rear side and have to be considered in an analysis, in contrast to Ref. 34. Additionally, the full-beam envelope is relatively round. The source size of the full beam is deduced to be  $(85 \pm 5)\ \mu\text{m}$  for these 5 MeV protons. This analysis was done for all RCF layers to obtain the full-beam source-size dependent energy distribution shown in Fig. 6. It can again be fitted to a Gaussian as in the case with a round laser focus. The FWHM of the source is  $92\ \mu\text{m}$ , that is larger than the source size with a round focus. The targets were made out of the same foil, so the increase in source size can only be a result of the larger laser focus. Larger absolute values of the source size were expected due to the larger laser focus. However, the round envelope, similar angle of beam-spread and ‘‘Gaussian-type’’ decrease with increasing energy as in the case with round foci shows, that the electron sheath envelope and acceleration was the same in both cases, independent of the laser beam profile. The laser beam profile nevertheless had an influence on the spatial beam profile, but it seems to have the character of an initial perturbation, bending the lines inside

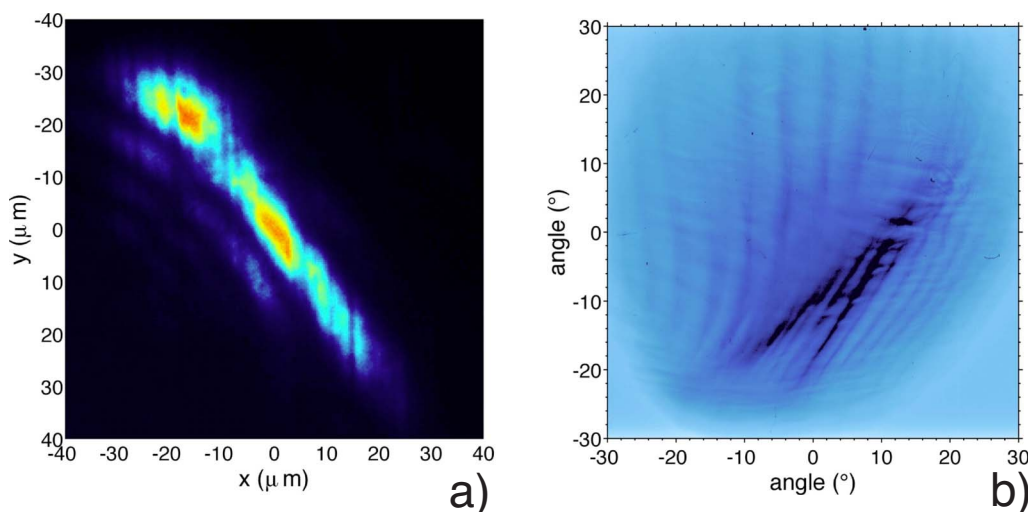


FIG. 5. (Color online) (a) Line laser focus profile with  $(80 \times 10)\ \mu\text{m}$  axes length that was used to irradiate a  $50\ \mu\text{m}$  Au foil. The laser energy was 15.3 J (LULI No. 26). (b) The resulting proton beam profile shows the laser imprinted ellipse and a relatively round beam with lines. The source size is  $75\ \mu\text{m}$ , and the size of the elliptical region is  $35\ \mu\text{m}$  in one direction.

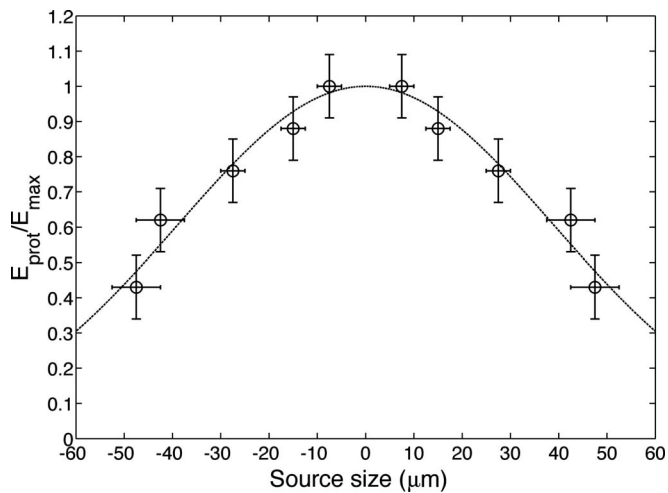


FIG. 6. (LULI No. 26) Source-size dependent energy distribution ( $\circ$ ) from the shot of Fig. 5. The energies are normalized to the current maximum energy of 11 MeV. Although the laser was shaped to a line focus, the proton beam was relatively round. A Gaussian fit (---) similar to Fig. 4 can be applied with a FWHM of  $92 \mu\text{m}$ .

due to a central nonradially symmetric part in a radially symmetric sheath.

We now examine the change of the proton beam profile with target thickness. The experiments were performed at the TRIDENT laser facility. The resulting proton beam profiles with an elliptical laser focus are shown in Fig. 7. The laser beam profile is shown in Fig. 7(a) with  $(108.5 \times 28) \mu\text{m}$  axes length and was the same for all shots, as well as the laser energy and pulse duration. For comparison we only show RCF images of 5 MeV protons. Figures 7(b)–7(d) show the results with the target thickness increasing from  $13 \mu\text{m}$  (b) via  $20 \mu\text{m}$  (c) to  $50 \mu\text{m}$  (d). The color map was optimized for maximum contrast of each film individually. For an enhanced visibility of the grooves imaged in the RCF, semitransparent lines have been overlapped in (b)–(d). In (d) the target was rotated as in Fig. 8. Whereas for thin targets ( $13 \mu\text{m}$ ) the elliptical laser beam profile is the most dominant part of the proton beam [see Fig. 7(b)], for thicker targets the elliptical part becomes less pronounced and the envelope becomes rounder. The source sizes of all 5 MeV

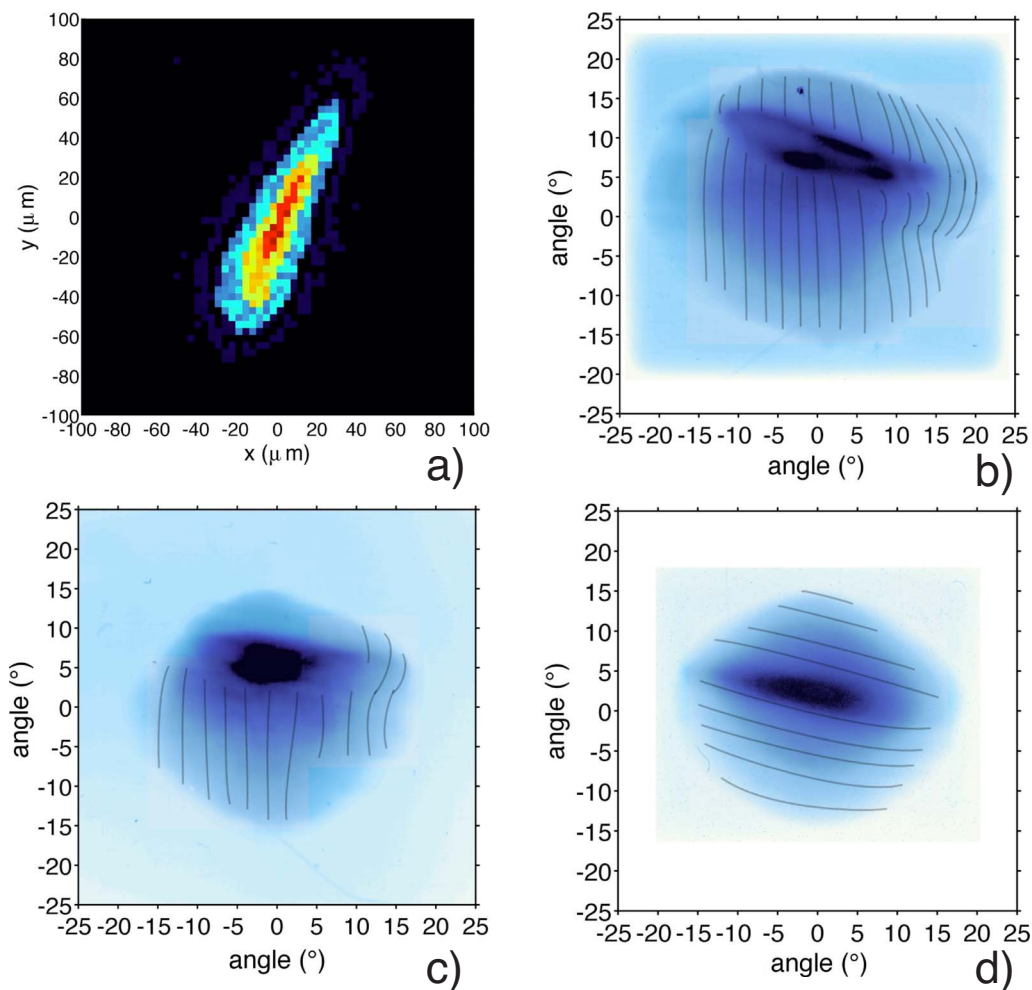


FIG. 7. (Color online) Influence of target thickness on proton beam profile. (a) The laser was defocused to an ellipse with eccentricity 4 and an intensity of  $2.5 \times 10^{18} \text{ W/cm}^2$ . (b) For a  $13 \mu\text{m}$  thick target the ellipse in the proton beam profile is clearly visible, and the image shows 5 MeV protons. The beam profile of the 5 MeV protons becomes more symmetric with increasing target thickness from  $20 \mu\text{m}$  (c) to  $50 \mu\text{m}$  (d), and the elliptical part moves to the center. In all three cases the laser focus was kept unchanged. For an enhanced visibility of the grooves imaged in the RCF, semitransparent lines have been overlapped in (b)–(d). In (d) the target was rotated as in Fig. 8.

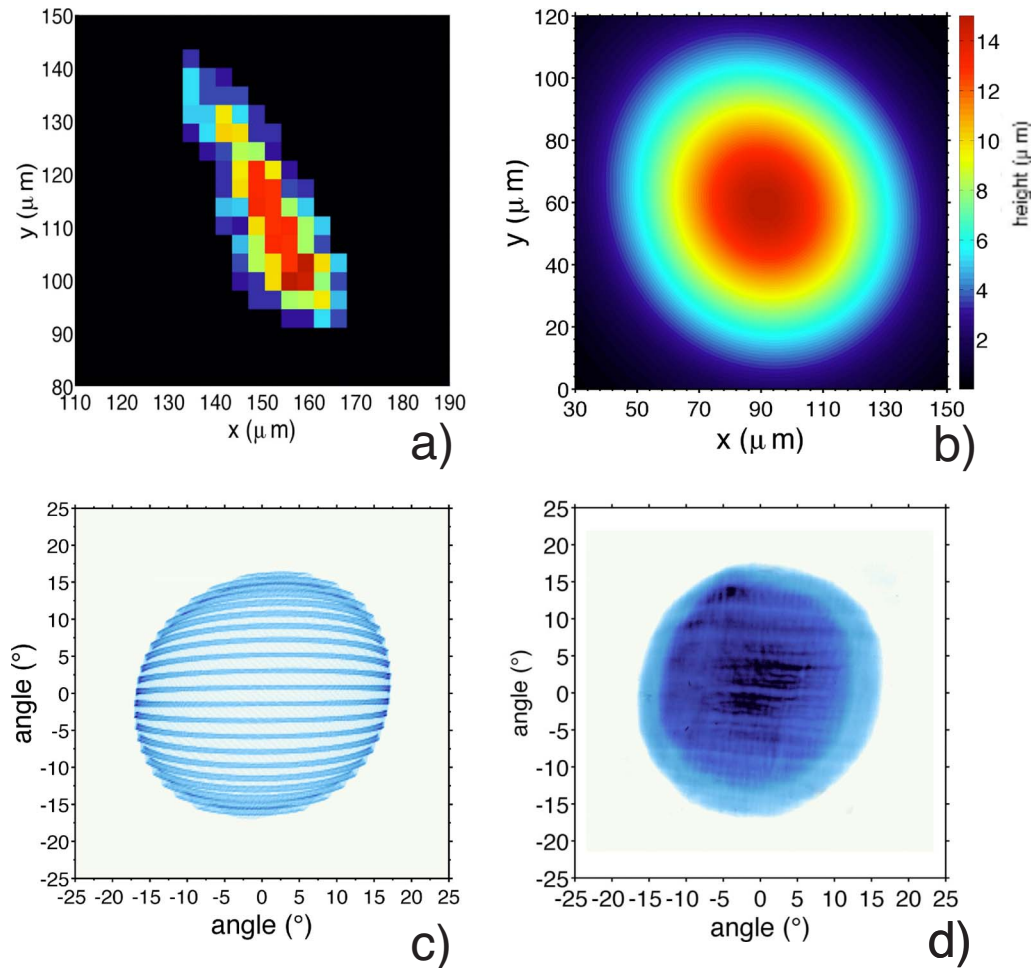


FIG. 8. (Color online) Simulated proton beam profile for a  $50\ \mu\text{m}$  thick Au target. The laser focus (a) is taken as an input parameter, and the intensity of this shot was  $7.3 \times 10^{18}\ \text{W}/\text{cm}^2$ , resulting in hot electrons with a temperature of 1 MeV. The broadening due to small-angle scattering leads to a smooth rear side electron distribution (b), which in turn shows a smooth simulated proton image (c) that closely reproduces the measured 5 MeV proton image (d). The  $15\ \mu\text{m}$  height of the sheath was fit so that the divergence of the simulated and measured beam overlaps. The ring visible in (d) is a result of the transmission scan through the two active layers in MD-55.

protons are  $(130 \pm 10)\ \mu\text{m}$ ,  $(110 \pm 30)\ \mu\text{m}$ , and  $(90 \pm 20)\ \mu\text{m}$  for the 13, 20, and  $50\ \mu\text{m}$  targets, respectively. It is interesting to note that the 5 MeV proton's source size *decreases* with target thickness. The divergent electron transport<sup>30,31</sup> should lead to an increasing source size with target thickness. The maximum energy was approximately 7 MeV in all three cases, but with weaker and smaller beam imprints of the maximum energy protons with target thickness. We cannot determine the maximum energy accurately, since the RCF stack's energy resolution of  $\approx 1\ \text{MeV}$  is weak and therefore is rather subject to error. We know from the experiments described above, that protons have a decreasing source size with increasing energy. In the case here the beam spot of protons slightly decreased with target thickness. Since we have only considered 5 MeV protons, independent of the maximum energy, we assume that the data for thicker targets represents protons closer to the maximum energy, therefore their source size must decrease with target thickness. The RCF stack's energy resolution was not sufficient to fit a Gaussian to the measured data, therefore we cannot deduce a FWHM source size as in the cases above. We can estimate it, however, since we know the source size of the

5 MeV protons and we know the maximum energy is between 6 and 8 MeV. Therefore 5 MeV energy represents protons between 62.5% and 83% of the maximum. We know their source size, so this allows us to calculate the FWHM source size. It is  $\approx (140 \pm 30)\ \mu\text{m}$  for the  $50\ \mu\text{m}$  target and  $\approx (200 \pm 45)\ \mu\text{m}$  for the  $13\ \mu\text{m}$  thin foil. Therefore we can conclude that the whole source size decreased with increasing target thickness, although the electrons have divergently propagated through the target, which resulted in a larger area of electron presence. Since there is no difference on the front side for all three cases, i.e., laser parameters as well as the target's front side were not changed, we can assume that the same amount of energy was transported from the laser to the rear side. However, for thicker targets the volume occupied by the electrons is larger, hence the electric field strength became less with increasing target thickness. Therefore 5 MeV energy was closer to the maximum with increasing thickness, which explains the decreasing source size with increasing thickness.

Additionally, the increasing target thickness results in a smoother proton beam profile with less impact of the laser beam profile, i.e., the elliptical part of the beam becomes less

pronounced, moves more to the center of the beam profile and the background becomes more symmetric with target thickness.

In summary, we have observed that the shape of the laser beam profile influences the intense part of laser-accelerated proton beam profiles, while the beam envelope stays relatively round. In addition to that, the resulting beam is smoothed and more symmetric the thicker the targets are. For an explanation of these findings we have developed a model that is described in the next section.

## A. Model

A full 3D model of the electron generation and transport in our experiments is beyond the capacity of current computer codes and needs a more simplified approach. We developed the Sheath-Accelerated Beam Ray-tracing for IoN Analysis code SABRINA, which calculates the shape of the proton distribution in the detector for a given laser beam profile. The physical picture is as follows.

The laser interacts with the electrons of the preplasma formed by the prepulse and transfers a large fraction of its energy to hot electrons.<sup>40</sup> The hot electrons are approximated by a Boltzmann distribution with a temperature (i.e., average kinetic energy) of

$$k_B T_{\text{hot}} = mc^2 \left( 1 + \frac{2U_p}{mc^2} \right)^{1/2}. \quad (1)$$

In this equation the following laser ponderomotive potential  $U_p$  is used:<sup>16</sup>  $U_p = 9.33 \times 10^{-14} I [\text{W}/\text{cm}^2] \lambda^2 [\mu\text{m}^2] \text{ eV}$ .

Since for the elongated astigmatic foci there is no simple way to obtain the intensity by taking just the FWHM, the intensity of the laser pulse was calculated by counting all pixels above 50% of the maximum. This value was used as the area of the focus. The intensity is then just the laser energy divided by the pulse duration and this area. It was assumed that the spatial distribution of the hot electrons closely follows the laser beam profile, with an average electron energy that was calculated with Eq. (1). The huge amount of MeV electrons results in a MA electron current that is transported through the target. Integrated 3D hybrid particle-in-cell (PIC) simulations of laser interaction and electron transport with thin foils (10  $\mu\text{m}$ ) show that the electrons propagate nearly ballistically through the target,<sup>28</sup> whereas 3D simulations by hybrid-PIC without laser-interaction and thicker foils<sup>47</sup> indicate a collimated transport guided by magnetic fields and possible filamentation of the electron current into beamlets. However, most of the experimental results (see Refs. 30 and 31 for a short summary) show a divergent electron transport. Therefore, and for simplicity, we neglect a possible collimation by a magnetic field. Nevertheless, due to the solid-state density of the cold target there will be collisions by the electrons with the background material that tend to broaden the electron current distribution. This contribution of multiple small-angle scattering leads to an angular broadening of the electrons. In this article we have used Molières theory of multiple scattering by Bethe<sup>41</sup> to calculate the broadening of the electrons. After passing the target the electrons form the dense sheath at the

rear side that accelerates the protons. In the framework of an electrostatic, quasineutral ideal two-fluid model<sup>42</sup> the electric field driving the expansion only depends on the gradient of the electron pressure tensor

$$E_{\text{es}} = \frac{-\nabla p_e}{en_{\text{hot}}} = -\frac{\nabla(n_{\text{hot}} k_B T_{\text{hot}})}{en_{\text{hot}}}. \quad (2)$$

The angular direction of the protons therefore depends on the gradient of the electron sheath,

$$\alpha_{\text{prot}} \propto \frac{\nabla n_{\text{hot}}}{n_{\text{hot}}}. \quad (3)$$

The algorithm takes the laser beam profile as an input. The broadening due to small-angle scattering is represented by convolving the electron distribution (i.e., the laser focus image) with a Gaussian angular distribution with a FWHM angle from Molières's theory at an energy that corresponds to  $T_{\text{hot}}$ . The result represents the electron sheath at the rear side; this is then divided into a grid. For each grid element the normal direction is then calculated. In our approximation of a quasineutral plasma the longitudinal electric field is proportional to the height of the sheath. Therefore the higher energy protons originate from the outer region (in longitudinal direction) of the sheath.

Similar to the model of Ruhl *et al.*,<sup>25</sup> the effect of the grooves at the rear side was included as a sinusoidal perturbation  $\delta\alpha$  in the angle of expansion,

$$\delta\alpha = A \sin\left(\frac{2\pi x}{\lambda}\right), \quad (4)$$

with a periodicity  $\lambda$  of 5  $\mu\text{m}$  or 10  $\mu\text{m}$  and an amplitude  $A$  fit to the data (the amplitude just controls the visibility of the lines). Depending on the initial line orientation at the target the perturbation was taken either in the  $x$ - or  $y$ -direction.

The height of the sheath cannot be calculated by taking the laser beam profile measurements. Since the protons expand in the direction of the sheath normal, we use the measured angle of beam spread to adjust the height of the sheath until the simulated beam fits the measured one. The model therefore allows us to reconstruct the shape of the plasma sheath that determines the proton's angular expansion.

## B. Application

Figure 8 shows the application of our model to an experiment with a 50  $\mu\text{m}$  Au foil that had 5  $\mu\text{m}$  grooves at the rear side. Figure 8(a) shows the measured laser focus with an intensity of  $7.3 \times 10^{18} \text{ W}/\text{cm}^2$ . The ponderomotive potential is 0.75 MeV, that results in a hot-electron temperature of 1 MeV. The full angular broadening of the hot electrons with a kinetic energy of 1 MeV then is 68° FWHM. We have assumed that only the upper 70% of the sheath contribute to the 5 MeV protons that were measured in the experiments. This value is motivated by the argument that protons above 5 MeV are between 62.5% and 83% of the maximum energy. It is worth noting that below 60% of the sheath, it has—due to the Gaussian shape—a reflection point that leads to rings in the image as pointed out by Brambrink *et al.*<sup>43</sup> Those rings were not seen in our experimental data.

The resulting distribution at the rear side is shown in Fig. 8(b). A best fit with SABRINA to the experiment is obtained by adjusting the height of this sheath to  $15\ \mu\text{m}$ ; see Figs. 8(c) and 8(d) for a comparison of 5 MeV protons. The height of  $15\ \mu\text{m}$  is comparable to values already published in the literature<sup>7</sup> and leads to an acceleration time on the order of a ps. In both model and experiment the source size can be deduced to be  $(95 \pm 15)\ \mu\text{m}$ . Although the broadening angle calculated by small-angle scattering reproduces this experimental data point, this value does not fit for different energies of the protons. The maximum proton energy was  $\approx 7\ \text{MeV}$  with a source size of  $65\ \mu\text{m}$ . As mentioned before, there could have been higher energy protons, above 7 MeV and below the detection threshold of the next RCF, with less source size. The 7 MeV protons' source size implies an electron transport cone angle of  $24^\circ$ , that is close to the value reported in Ref. 34 with a similar target but for a lower proton energy. However, a SABRINA simulation with this small angle does not reproduce the measured beam profile. The measured profile instead can be reproduced by taking the broadening of  $68^\circ$  FWHM and only the upper 5% of the resulting rear side sheath. A test with different shots indeed shows that beam profiles for the highest-energy protons can be reproduced by taking only the upper few percent of the simulated sheath profile. The profiles for lower energetic protons then can be simulated by subsequently taking more of the sheath.

This leads to the following physical picture: The electron sheath is fully developed before significant expansion of the protons occurs. The protons with the highest energy are accelerated by the strongest part of the electric field that has its maximum in the center. The accelerating electric field amplitude decays like a Gaussian in the transverse direction, therefore lower energy protons originate from larger sources, see Fig. 4. The height of the sheath determines the angular expansion.

Next we compare this model with data from experiments with  $13\ \mu\text{m}$  thick Au foils. We try to reproduce an experimental result from TRIDENT ( $I=2.5 \times 10^{18}\ \text{W}/\text{cm}^2$ ,  $U_{\text{pond}}=0.26\ \text{MeV}$ ,  $T_{\text{hot}}=0.7\ \text{MeV}$ ). The angular broadening due to multiple small-angle scattering is  $42^\circ$  FWHM. Figure 9(a) shows the measured laser beam profile. The proton beam profile is shown in Fig. 9(b). Despite the ellipse due to the laser beam profile the lower part of the image shows vertical lines from the grooved target surface. The source size of this part is  $130\ \mu\text{m}$ . In the upper part the former vertical lines were bent to the left, and they have less contrast than the lines in the lower part. The large source size would imply a very large electron transport cone angle of  $148^\circ$  FWHM, that is more than two times the angle by small-angle scattering. Indeed, neither a SABRINA simulation with broadening due to small-angle scattering only [see Fig. 9(c)] nor a simulation with  $148^\circ$  broadening [Fig. 9(d)] coincide with the measured data. The shape of the image produced by the small-angle scattering calculation roughly fits the intense elliptical part of the measured data. The round part is reasonably reproduced by the calculation with the large cone angle.

This could imply that two different proton beams overlap in the temporally integrating detector. If there had been

two temporally separated populations however, the straight lines from the large angle part should overlap with the elliptical part and should be visible everywhere in the measured data. A close inspection does not show any lines in the elliptical part, although the RCF was not saturated. Instead, there is a slight bending of the lines, that was even more visible in different shots. Therefore we conclude that the image was not produced by two different proton beams.

The measurements can be approximated however, by keeping the broadening of  $42^\circ$  by small-angle scattering and additionally by magnifying (interpolating) the laser focus image up to the measured source size. This results in a rear-side sheath that follows the laser beam topology. Figure 9(e) shows the sheath, the height of  $200\ \mu\text{m}$  was fit to result in a beam divergence that matches the measured data. The resulting proton beam profile is shown in Fig. 9(f) and shows a reasonable agreement with the experiment. For this reproduction of the beam profile the source size had to be increased by a factor of 3. The most energetic protons of this shot had an energy of 7 MeV with a source size of  $80\ \mu\text{m}$ . Again a SABRINA simulation shows that only the case where we take the upper 5% of the sheath that was fit to the 5 MeV protons shows good agreement. We find the same for thin targets compared to thick ones for the experiments at LULI: Our model can be used to reproduce the shape and source size of laser-accelerated protons for thick targets. For thin targets we can estimate the shape of the sheath by the assumption of multiple small-angle scattering, too. However, the size of the resulting sheath must be increased several times (up to a factor 5) to match the measured source sizes.

#### IV. DISCUSSION

There are several physical mechanisms that can be responsible for the large source sizes that were measured with thin targets. First there could be some transverse spreading of the electrons at the rear side, as reported recently by McKenna *et al.*<sup>44</sup> The velocity of the spreading observed there is constant with  $\approx 3/4c$  (where  $c$  is the speed of light in vacuum). The sheath for TRIDENT in the section above, is about twice the size of the laser focus. This would correspond to a time duration of the electron spreading of  $50\ \mu\text{m}/2.25 \times 10^8\ \text{m/s}=222\ \text{fs}$  if we assume a uniform electron velocity. This is a factor of 4 less than the laser pulse duration, so it seems to have no relation with the laser. Additionally, a constant spread velocity of the sheath would result in an isotropization of the elongated sheath, since the thin side will—relatively to its initial size—expand much more than the long side, leading to a decrease in aspect ratio. The SABRINA simulation from above, however, shows that the aspect ratio of the sheath closely follows the laser beam. Therefore a transverse spread as reported in Ref. 44 seems to not explain the results in this work.

Another possibility could be the existence of two different electron populations like those measured by Gremillet *et al.*<sup>45</sup> and just recently by Santos *et al.*<sup>46</sup> They report about a fast, strongly collimated (jetlike) hot MeV-electron beam and a second, much broader electron bulk component. Although their measurements were either done with insulating glass

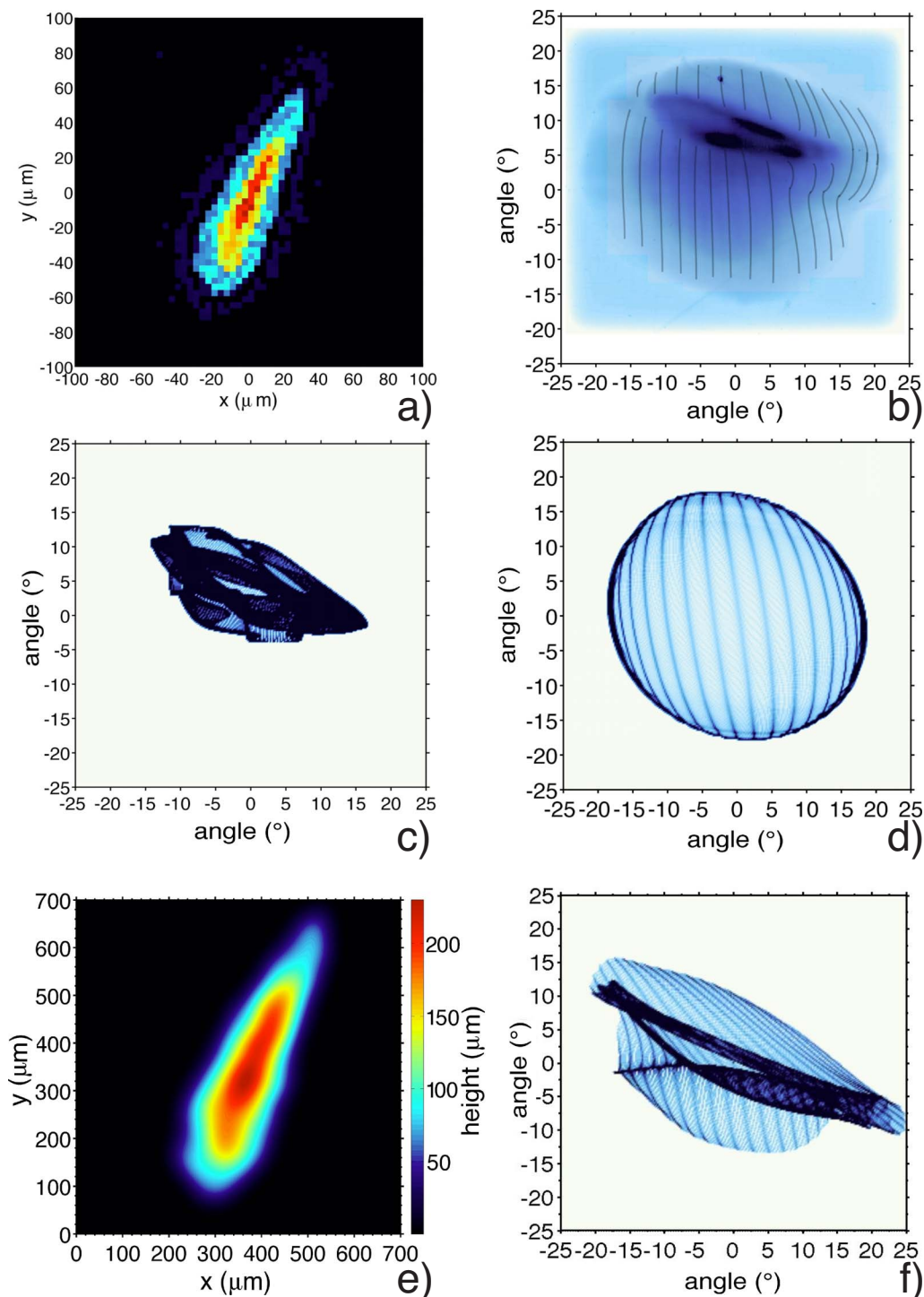


FIG. 9. (Color online) Simulated images for a thin  $13\ \mu\text{m}$  Au target. (a) The laser focus was taken as an input, and (b) shows the measured beam profile for 5 MeV protons. Semitransparent lines have been overlapped to enhance the visibility of the grooves imaged in the RCF. (c) The simulation with broadening due to small-angle scattering only shows a strongly deformed proton beam profile, (d) whereas a broadening with  $\alpha=148^\circ$  up to the measured source size of  $130\ \mu\text{m}$  shows a beam without ellipse. (e) The measurements can be simulated, however, by magnifying (interpolating) the laser focus image to the measured source size and by taking a broadening due to small-angle scattering for homogenization. This results in a rear-side sheath that closely follows the laser beam topology. The height of  $200\ \mu\text{m}$  was fit to result in a beam divergence that fits to the measured data. (f) The resulting proton beam profile shows a reasonable agreement with the experiment.

targets at high laser energy<sup>45</sup> or aluminum foils at low laser energy,<sup>46</sup> two electron populations could exist in our experiments at high laser energy and gold foils, too. Both electron populations expand fast enough to overlap at the rear side and could contribute to the proton acceleration. However, as

stated by Ref. 46 the collimated feature contains only very little energy around 1% of the laser energy, compared to the 35% energy contained in the bulk part. In addition to that is the bulk's divergence angle of  $35^\circ \pm 5^\circ$  determined there too small to explain the findings in our experiments.

In this discussion we should not forget the influence of the front-side injection and recirculation of the hot electrons. Since the sheath field at the rear side is convex (e.g., like a Gaussian), it can act as a weak focusing lens for the reflected electrons. At the front side they can either enter the area of the laser focus again or they will be pushed back into the target by the charge-separation field at the front side. This can lead to an increase of the sheath density and temperature, hence to an increase of the electric field. Electrons with a velocity close to the speed of light can travel back and forth (reflux) of the thin target for about 10 times during the laser pulse duration of  $\approx 1$  ps. The range of 1 MeV electrons in (cold) gold is  $\approx 150 \mu\text{m}$ ,<sup>48</sup> so the electrons keep refluxing when the laser is off until their energy is lost. Recirculation effects are much less important for the thick targets where the electrons travel only 3 times through a  $50 \mu\text{m}$  foil while the laser is on. Measurements and modeling of Cu  $K_\alpha$  x-ray emission and electron transport by irradiating copper foils with similar intensities as in this article support this argument.<sup>49,50</sup> Additionally it is possible that the electrons were injected with a certain angular distribution. The injection depends on the preplasma profile as well as on the laser beam topology and therefore is hard to estimate and needs a fully detailed three-dimensional computer simulation.

## V. CONCLUSION AND OUTLOOK

In summary, we reported about protons accelerated from thin, microstructured gold foils with nonaxially symmetric laser-beam foci. The asymmetric laser beam results in asymmetric proton beam profiles. The energy resolved source size of the protons was deduced by imaging the beam perturbations from the microgrooved surface into a RCF detector stack. It was shown that the protons with the highest energies were emitted from the smallest source. When the laser focus size was increased, the proton source size increased as well. For symmetric as well as asymmetric laser beam profiles, the source-size dependent energy distribution in both cases could be fit to a Gaussian. This led to the conclusion that the laser beam profile has no significant contribution to the general expansion characteristics of laser-accelerated protons, but it can strongly modify the transverse beam profile without changing the angle of the beam spread.

For a more detailed analysis of the experimental results we developed the Sheath-Accelerated Beam Ray-tracing for IoN Analysis code SABRINA, which takes the laser beam parameters as input and calculates the shape of the proton distribution in the detector. The electron transport was modeled to closely follow the laser beam profile topology and a broadening due to small-angle collisions was assumed. It was shown that broadening due to small-angle collisions is the major effect to describe the source size of protons for thick target foils ( $50 \mu\text{m}$ ). In contrast to that, thin target foils ( $13 \mu\text{m}$ ) show much larger sources than expected due to small-angle collisions. The physical reason behind this observation stays unclear and is most likely the result of electron refluxing.

We conclude that the shape of the sheath at the rear side of the thick targets can be estimated by a simple model of

broadening due to multiple small-angle scattering, but it fails for the description of the sheath broadening in thin targets. However, a clear answer of the physical mechanism behind the large source sizes and sheath profiles can only be obtained by a full-scale integrated three-dimensional computer simulation that contains the laser-plasma interaction as well as the electron transport, which is beyond the possibilities of this work and is left for the future.

The results obtained in this work are useful for optimization of applications as, e.g., proton radiography or proton fast-ignition (PFI). In proton radiography a homogeneous smooth beam profile without modulations is necessary. Thick targets lead to homogenization of the proton beam profile, but the sheath becomes weaker and therefore the maximum obtainable energy is reduced, hence the temporal resolution due to the time-of-flight of the proton beam radiography becomes worse. Thin targets however increase the maximum proton energy, but the influence of the laser beam focus on the proton beam profile is much stronger and sheath broadening leads to source sizes that are comparable to source sizes of thick foils.

We have shown that the imprint of the laser beam profile affects the intense part of the proton beam profile. This effect must be present in cases with a round focal spot, too. Therefore a focal spot with a sharp peaked laser beam profile will result in a strongly divergent proton beam as observed in the experiments. The findings also explain that in cases where a collimation of the proton beam is required, e.g., PFI or the injection of the beam into a postaccelerator, not only a curved target surface<sup>51,52</sup> is necessary, but a large, flattop laser focal spot is indispensable to produce a flat proton-accelerating sheath.

## ACKNOWLEDGMENTS

We gratefully acknowledge the excellent support by the TRIDENT and LULI laser teams. M.S. wants to thank H. Ruhl for fruitful discussions and support. We thank IMVT, Forschungszentrum Karlsruhe, as well as IHT, TU Darmstadt, for parts of the target preparation.

This work was performed within the Virtual Institute VI-VH 144 (VIPBUL) funded by the Helmholtz Association. B.M.H., K.A.F., J.C.F., and D.C.G. were funded by the U.S. DOE through the LDRD program, Grant No. 20040064. Sandia is a multiprogram laboratory operated by Sandia Corporation, a Lockheed Martin Company, for the United States Department of Energy under Contract No. DE-AC04-94AL85000.

<sup>1</sup>R. A. Snavely, M. H. K. S. P. Hatchett, T. E. Cowan, M. Roth, T. W. Phillips, M. A. Stoyer, E. A. Henry, T. C. Sangster, M. S. Singh, S. C. Wilks, A. MacKinnon, A. Offenberger, D. M. Pennington, K. Yasuike, A. B. Langdon, B. F. Lasinski, J. Johnson, M. D. Perry, and E. M. Campbell, *Phys. Rev. Lett.* **85**, 2945 (2000).

<sup>2</sup>E. L. Clark, K. Krushelnick, J. R. Davies, M. Zepf, M. Tatarakis, F. N. Beg, A. Machacek, P. A. Norreys, M. I. K. Santala, I. Watts, and A. E. Dangor, *Phys. Rev. Lett.* **84**, 670 (2000).

<sup>3</sup>A. Maksimchuk, S. Gu, K. Flippo, D. Umstadter, and V. Yu. Bychenkov, *Phys. Rev. Lett.* **84**, 4108 (2000).

<sup>4</sup>S. P. Hatchett, C. G. Brown, T. E. Cowan, A. Henry, J. S. Johnson, M. H. Key, J. A. Koch, A. B. Langdon, B. F. Lasinski, R. W. Lee, A. J. Mackinnon, D. M. Pennington, M. D. Perry, T. W. Phillips, R. T. C. Sangster, M.

- S. Singh, R. A. Snavely, M. A. Stoyer, S. C. Wilks, and K. Yasuike, *Phys. Plasmas* **7**, 2076 (2000).
- <sup>5</sup>M. Borghesi, D. H. Campbell, A. Schiavi, M. G. Haines, O. Willi, A. J. MacKinnon, P. Patel, L. A. Gizzi, M. Galimberti, R. J. Clarke, F. Pegoraro, H. Ruhl, and S. Bulanov, *Phys. Plasmas* **9**, 2214 (2002).
- <sup>6</sup>A. J. MacKinnon, P. K. Patel, M. Borghesi, R. C. Clarke, R. R. Freeman, H. Habara, S. P. Hatchett, D. Hey, D. G. Hicks, S. Kar, M. H. Key, J. A. King, K. Lancaster, D. Neely, A. Nikkro, P. A. Norreys, M. M. Notley, T. W. Phillips, L. Romagnani, R. A. Snavely, R. B. Stephens, and R. P. J. Town, *Phys. Rev. Lett.* **97**, 045001 (2006).
- <sup>7</sup>L. Romagnani, J. Fuchs, M. Borghesi, P. Antici, P. Audebert, F. Ceccherini, T. Cowan, T. Grismayer, S. Kar, A. Macchi, P. Mora, G. Pretzler, A. Schiavi, T. Toncian, and O. Willi, *Phys. Rev. Lett.* **95**, 195001 (2005).
- <sup>8</sup>M. I. K. Santala, M. Zepf, F. N. Beg, E. L. Clark, A. E. Dangor, K. Krushelnick, M. Tatarakis, I. Watts, K. W. D. Ledingham, T. McCanny, I. Spencer, A. C. Machacek, R. Allott, R. J. Clarke, and P. A. Norreys, *Appl. Phys. Lett.* **78**, 19 (2001).
- <sup>9</sup>A. Pukhov, *Phys. Rev. Lett.* **86**, 3562 (2001).
- <sup>10</sup>M. Roth, T. E. Cowan, M. H. Key, S. P. Hatchett, C. Brown, W. Fountain, J. Johnson, D. M. Pennington, R. A. Snavely, S. C. Wilks, K. Yasuike, H. Ruhl, F. Pegoraro, S. V. Bulanov, E. M. Campbell, M. D. Perry, and H. Powell, *Phys. Rev. Lett.* **86**, 436 (2001).
- <sup>11</sup>M. Hegelich, S. Karsch, G. Pretzler, D. Habs, K. Witte, W. Guenther, M. Allen, A. Blazevic, J. Fuchs, J. C. Gauthier, M. Geissel, P. Audebert, T. Cowan, and M. Roth, *Phys. Rev. Lett.* **89**, 085002 (2002).
- <sup>12</sup>K. A. Flippo, B. M. Hegelich, M. J. Schmitt, D. C. Gauthier, C. A. Meserole, G. L. Fisher, J. A. Cobble, R. A. Johnson, S. A. Letzring, J. C. Fernandez, M. Schollmeier, and J. Schreiber, *Proc. SPIE* **6261**, 62612I (2006).
- <sup>13</sup>K. A. Flippo, B. M. Hegelich, M. J. Schmitt, C. A. Meserole, G. L. Fisher, D. C. Gautier, J. A. Cobble, R. Johnson, S. Letzring, J. Schreiber, M. Schollmeier, and J. C. Fernandez, *J. Phys. IV* **133**, 1117 (2006).
- <sup>14</sup>J. C. Fernandez, B. M. Hegelich, J. A. Cobble, K. A. Flippo, S. A. Letzring, R. P. Johnson, D. C. Gautier, T. Shimada, G. A. Kyrala, Y. Q. Wang, C. J. Wetteland, and J. Schreiber, *Laser Part. Beams* **23**, 267 (2005).
- <sup>15</sup>S. J. Gitomer, R. D. Jones, F. Begay, A. W. Ehler, J. F. Kephart, and R. Kristal, *Phys. Fluids* **29**, 2679 (1986).
- <sup>16</sup>S. C. Wilks, A. B. Langdon, T. E. Cowan, M. Roth, M. Singh, S. Hatchett, M. H. Key, D. Pennington, A. MacKinnon, and R. A. Snavely, *Phys. Plasmas* **8**, 542 (2001).
- <sup>17</sup>J. Fuchs, P. Antici, E. d'Humières, E. Lefebvre, M. Borghesi, E. Brambrink, C. A. Cecchetti, M. Kaluza, V. Malka, M. Manclossi, S. Meyroneinc, P. Mora, J. Schreiber, T. Toncian, H. Pepin, and P. Audebert, *Nat. Phys.* **2**, 48 (2006).
- <sup>18</sup>Y. Oishi, T. Nayuki, T. Fujii, Y. Takizawa, X. Wang, T. Yamazaki, K. Nemoto, T. Kayojii, T. Sekiya, K. Horioka, Y. Okano, Y. Hironaka, K. G. Nakamura, K. Kondo, and A. A. Andreev, *Phys. Plasmas* **12**, 073102 (2005).
- <sup>19</sup>P. Antici, J. Fuchs, E. d'Humières, E. Lefebvre, M. Borghesi, E. Brambrink, C. A. Cecchetti, S. Gaillard, L. Romagnani, Y. Sentoku, T. Toncian, O. Willi, P. Audebert, and H. Pepin, *Phys. Plasmas* **14**, 030701 (2007).
- <sup>20</sup>M. S. Wei, J. R. Davies, E. L. Clark, F. N. Beg, A. Gopal, M. Tatarakis, L. Willingale, P. Nilson, A. E. Dangor, P. A. Norreys, M. Zepf, and K. Krushelnick, *Phys. Plasmas* **13**, 123101 (2006).
- <sup>21</sup>M. Schnürer, S. Ter-Avetisyan, P. V. Nickles, and A. A. Andreev, *Phys. Plasmas* **14**, 033101 (2007).
- <sup>22</sup>T. E. Cowan, J. Fuchs, H. Ruhl, A. Kemp, P. Audebert, M. Roth, R. Stephens, I. Barton, A. Blazevic, E. Brambrink, J. Cobble, J. Fernandez, J.-C. Gauthier, M. Geissel, M. Hegelich, J. Kaae, S. Karsch, G. P. Le Sage, S. Letzring, M. Manclossi, S. Meyroneinc, A. Newkirk, H. Pepin, and N. Renard-LeGalloudec, *Phys. Rev. Lett.* **92**, 204801 (2004).
- <sup>23</sup>E. Brambrink, J. Schreiber, T. Schlegel, P. Audebert, J. Cobble, J. Fuchs, M. Hegelich, and M. Roth, *Phys. Rev. Lett.* **96**, 154801 (2006).
- <sup>24</sup>A. J. Kemp, J. Fuchs, Y. Sentoku, V. Sotnikov, M. Bakeman, P. Antici, and T. E. Cowan, *Phys. Rev. E* **75**, 056401 (2007).
- <sup>25</sup>H. Ruhl, T. E. Cowan, and J. Fuchs, *Phys. Plasmas* **11**, L17 (2004).
- <sup>26</sup>M. Schollmeier, M. Roth, A. Blazevic, E. Brambrink, J. A. Cobble, J. C. Fernandez, K. A. Flippo, D. C. Gautier, D. Habs, K. Harres, B. M. Hegelich, T. Heßling, D. H. H. Hoffmann, S. Letzring, F. Nürnberg, G. Schaumann, J. Schreiber, and K. Witte, *Nucl. Instrum. Methods Phys. Res. A* **577**, 186 (2007).
- <sup>27</sup>D. C. Carroll, P. McKenna, O. Lundh, F. Lindau, C.-G. Wahlström, S. Bandyopadhyay, D. Pepler, D. Neely, S. Kar, P. T. Simpson, K. Markey, M. Zepf, C. Bellei, R. G. Evans, R. Redaelli, D. Batani, M. H. Xu, and Y. T. Li, *Phys. Rev. E* **76**, 065401 (2007).
- <sup>28</sup>D. R. Welch, D. V. Rose, M. E. Cuneo, R. B. Campbell, and T. A. Mehlhorn, *Phys. Plasmas* **13**, 063105 (2006).
- <sup>29</sup>E. d'Humières, E. Lefebvre, L. Gremillet, and V. Malka, *Phys. Plasmas* **12**, 062704 (2005).
- <sup>30</sup>K. L. Lancaster, J. S. Green, D. S. Hey, K. U. Akli, J. R. Davies, R. J. Clarke, R. R. Freeman, H. Habara, M. H. Key, R. Kodama, K. Krushelnick, C. D. Murphy, M. Nakatsutsumi, P. Simpson, R. Stephens, C. Stoeckl, T. Yabuuchi, M. Zepf, and P. A. Norreys, *Phys. Rev. Lett.* **98**, 125002 (2007).
- <sup>31</sup>J. S. Green, V. M. Ovchinnikov, R. G. Evans, K. U. Akli, H. Azechi, F. N. Beg, C. Bellei, R. R. Freeman, H. Habara, R. Heathcote, M. H. Key, J. A. King, K. L. Lancaster, N. C. Lopes, T. Ma, A. J. MacKinnon, K. Markey, A. McPhee, Z. Najmudin, P. Nilson, R. Onofrei, R. Stephens, K. Takeda, K. A. Tanaka, W. Theobald, T. Tanimoto, J. Waugh, L. Van Woerkom, N. C. Wooley, M. Zepf, J. R. Davies, and P. A. Norreys, *Phys. Rev. Lett.* **100**, 015003 (2008).
- <sup>32</sup>J. J. Santos, F. Amiranoff, S. D. Baton, L. Gremillet, M. Koenig, E. Martinolli, M. Rabec Le Gloahec, C. Rousseaux, D. Batani, A. Bernardinello, G. Greison, and T. Hall, *Phys. Rev. Lett.* **89**, 025001 (2002).
- <sup>33</sup>R. B. Stephens, R. A. Snavely, Y. Aglitskiy, F. Amiranoff, S. Andersen, D. Batani, S. D. Baton, T. Cowan, R. R. Freeman, T. Hall, S. P. Hatchett, J. M. Hill, M. H. Key, J. A. King, J. A. Koch, M. Koenig, A. J. MacKinnon, K. L. Lancaster, E. Martinolli, P. Norreys, E. Perelli-Cippo, M. Rabec Le Gloahec, C. Rousseaux, J. J. Santos, and F. Scianitti, *Phys. Rev. E* **69**, 066414 (2004).
- <sup>34</sup>J. Fuchs, T. E. Cowan, P. Audebert, H. Ruhl, L. Gremillet, A. Kemp, M. Allen, A. Blazevic, J.-C. Gauthier, M. Geissel, M. Hegelich, S. Karsch, P. Parks, M. Roth, Y. Sentoku, R. Stephens, and E. M. Campbell, *Phys. Rev. Lett.* **91**, 255002 (2003).
- <sup>35</sup>M. Kaluza, J. Schreiber, M. I. K. Santala, G. D. Tsakiris, K. Eidmann, J. Meyer-ter-Vehn, and K. J. Witte, *Phys. Rev. Lett.* **93**, 045003 (2004).
- <sup>36</sup>J. Schreiber, F. Bell, F. Grüner, U. Schramm, M. Geissler, M. Schnürer, S. Ter-Avetisyan, B. M. Hegelich, J. Cobble, E. Brambrink, J. Fuchs, P. Audebert, and D. Habs, *Phys. Rev. Lett.* **97**, 045005 (2006).
- <sup>37</sup>F. Nürnberg, Master's Thesis, Technische Universität Darmstadt, Darmstadt, 2006.
- <sup>38</sup>GAFchromic radiochromic film types HD-810 and MD-55 are trademarks of ISP corporation.
- <sup>39</sup>J. F. Ziegler, J. P. Biersack, and U. Littmark, *The Stopping and Range of Ions in Solids* (Pergamon, New York, 1985), <http://www.srim.org>.
- <sup>40</sup>M. H. Key, M. D. Cable, T. E. Cowan, K. G. Estabrook, B. A. Hammel, S. P. Hatchett, E. A. Henry, D. E. Hinkel, J. D. Kilkeny, J. A. Koch, W. L. Kruer, A. B. Langdon, B. F. Lasinski, R. W. Lee, B. J. MacGowan, A. MacKinnon, J. D. Moody, M. J. Moran, A. A. Offenberger, D. M. Pennington, M. D. Perry, T. J. Phillips, T. C. Sangster, M. S. Singh, M. A. Stoyer, M. Tabak, G. L. Tietbohl, M. Tsukamoto, K. Wharton, and S. C. Wilks, *Phys. Plasmas* **5**, 1966 (1998).
- <sup>41</sup>H. A. Bethe, *Phys. Rev.* **89**, 1256 (1953).
- <sup>42</sup>A. V. Gurevich, L. V. Pariiskaya, and L. P. Pitaevskii, *Sov. Phys. JETP* **22**, 449 (1966).
- <sup>43</sup>E. Brambrink, M. Roth, A. Blazevic, and T. Schlegel, *Laser Part. Beams* **24**, 163 (2006).
- <sup>44</sup>P. McKenna, D. C. Carroll, R. J. Clarke, R. G. Evans, K. W. D. Ledingham, F. Lindau, O. Lundh, T. McCanny, D. Neely, A. P. L. Robinson, L. Robson, P. T. Simpson, C.-G. Wahlström, and M. Zepf, *Phys. Rev. Lett.* **98**, 145001 (2007).
- <sup>45</sup>L. Gremillet, F. Amiranoff, S. D. Baton, J.-C. Gauthier, M. Koenig, E. Martinolli, F. Pisani, G. Bonnaud, C. Lebourg, C. Rousseaux, C. Toupin, A. Antonucci, D. Batani, A. Bernardinello, T. Hall, D. Scott, P. Norreys, H. Bandulet, and H. Pepin, *Phys. Rev. Lett.* **83**, 5015 (1997).
- <sup>46</sup>J. J. Santos, A. Debayle, Ph. Nicolaï *et al.*, *Phys. Plasmas* **14**, 103107 (2007).
- <sup>47</sup>J. J. Honrubia, M. Kaluza, J. Schreiber, G. D. Tsakiris, and J. Meyer-ter-Vehn, *Phys. Plasmas* **12**, 052708 (2005).
- <sup>48</sup>R. K. Batra and M. L. Sehgal, *Phys. Rev. B* **23**, 4448 (1981).
- <sup>49</sup>K. U. Akli, M. H. Key, H. K. Chung, S. B. Hansen, R. R. Freeman, M. H. Chen, G. Gregori, S. Hatchett, D. Hey, N. Izumi, J. King, J. Kuba, P. Norreys, A. J. MacKinnon, C. D. Murphy, R. Snavely, R. B. Stephens, C. Stoeckl, W. Theobald, and B. Zhang, *Phys. Plasmas* **14**, 023102 (2007).
- <sup>50</sup>W. Theobald, K. Akli, R. Clarke, J. A. Delettrez, R. R. Freeman, S. Glen-

zer, J. Green, G. Gregori, R. Heathcote, N. Izumi, J. A. King, J. A. Koch, J. Kuba, K. Lancaster, A. J. MacKinnon, M. Key, C. Mileham, J. Myatt, D. Neely, P. A. Norreys, H.-S. Park, J. Pasley, P. Patel, S. P. Regan, H. Sawada, R. Shepherd, R. Snavely, R. B. Stephens, C. Stoeckl, M. Storm,

B. Zhang, and T. C. Sangster, [Phys. Plasmas](#) **13**, 043102 (2006).

<sup>51</sup>P. K. Patel, A. J. MacKinnon, and M. H. Key, [Phys. Rev. Lett.](#) **91**, 125004 (2003).

<sup>52</sup>M. H. Key, [Phys. Plasmas](#) **14**, 055502 (2007).